Journal of Materials Chemistry C

PAPER

View Article Online
View Journal | View Issue

Cite this: J. Mater. Chem. C, 2016, 4, 10032

Large scale, highly efficient and self-powered UV photodetectors enabled by all-solid-state n-TiO_2 nanowell/p-NiO mesoporous nanosheet heterojunctions†

Lingxia Zheng, Feng Teng, Zhiming Zhang, Bin Zhao and Xiaosheng Fang*

Received 4th September 2016,
Accepted 28th September 2016

DOI: 10.1039/c6tc03830a

www.rsc.org/MaterialsC

Self-powered UV photodetectors (PDs) functioning without any power supply are urgently needed in modern optoelectronic devices from the viewpoint of being energy saving, portable and miniature. In this work, we report a novel heterojunction structure on a large scale based on n-type TiO_2 nanowells and p-type NiO mesoporous nanosheets in an economic route. The novel synthesis strategy using thin-layers of TiO_2 nanowells instead of conventional anodic nanotube geometry enables faster charge carrier transport through a shorter diffusion pathway along the lateral direction; and the flower-like morphology of NiO nanosheets guarantees the interfacial active reaction sites to UV light exposure, which takes great advantages of the p–n junction area to enhance the generation of electron–hole pairs. The hybrid PD performed in a self-powered mode is carefully explored which shows an enhanced photoresponse including good responsivity, excellent wavelength selectivity and high stability. This work presented here opens up new avenues for developing high-performance energy-efficient devices economically with a large area.

Introduction

UV photodetectors (PDs), which convert UV radiation signals to electronic ones, have been capturing intensive attention for a variety of industrial and military applications, including optical communications,[1] environment monitoring,[2] chemical/biological sensing,[3–5] future memory storage[6–8] and optoelectronic circuits.[9,10] In particular, UV PDs operating without consuming an external power source, namely self-powered UV PDs, are urgently needed to meet the evolution of modern electronic systems in the trend of being energy saving, portable and miniature.[9,11] For example, the self-powered PDs are essentially desirable for astronautical exploration, as the extra weight of the electrical power source will dramatically increase the launch cost.[12] To date, great progress has been made in fabricating self-powered UV PDs through the construction of p–n junctions, Schottky junctions and heterojunctions due to the efficient separation ability of photo-excited electron–hole pairs by the photovoltaic effect.[9,11–17] However, many problems still exist in these devices, such as complicated and expensive preparation processes, large lattice mismatch between hybrid materials and also the difficulty in scaling up for a large-area manufacture. Thus, an economic strategy is highly desirable to fabricate high performance self-powered UV PDs on a large scale.

Nowadays, the use of low-dimensional wide-bandgap semiconductor nanomaterials, such as ZnO,[18] TiO_2,[19] SnO_2,[20] ZnS,[21,22] Nb_2O_5[23] and GaN,[14] has attracted intense attention to develop high performance UV PDs.[10] Among them, TiO_2 is an increasingly well-studied semiconductor material for considerable energy- and environment-related applications owing to its biocompatibility, high stability and wide commercial availability.[24–26] Especially, with a wide bandgap ($\sim$3.2 eV for anatase), TiO_2 exhibits distinct UV absorption characteristics, making it an ideal candidate for visible-blind UV light sensors.[19,27,28] Although various TiO_2-based self-powered photoelectrochemical cell (PEC) type detectors have been investigated recently,[29–32] they always suffer from the evaporation of electrolytes, resulting in a short working life limiting the practical applications. In addition, due to the fast recombination of photogenerated electron–hole pairs in TiO_2 and the slow oxygen adsorption/desorption processes, the photoresponse times for all-solid-state TiO_2-based PDs tend to be very slow (even tens of minutes).[19] Thus, much work needs to be conducted to develop all-solid-state, fast response speed self-powered TiO_2-based PDs. According to previous studies,[13,33–35] nickel oxide (NiO) as a typical wide-bandgap material ($E_g \approx 3.5$ eV) is extensively used in the construction of a p–n junction owing to its high hole mobility, high p-type concentration and low

Department of Materials Science, Fudan University, Shanghai 200433, P. R. China. E-mail: xshfang@fudan.edu.cn

† Electronic supplementary information (ESI) available: SEM images, *I–V* and *I–t* curves. See DOI: 10.1039/c6tc03830a

cost production. The TiO_2/NiO heterostructures are well-demonstrated in a variety of applications, such as water splitting, photocatalysts, supercapacitors and lithium ion batteries,[36–40] due to their superior separation capability of photogenerated electron–hole pairs. Nevertheless, the self-powered UV PDs based on TiO_2/NiO p–n junctions are still scarce.

Herein, we demonstrate a hybrid PD functioning in a self-powered mode by constructing heterojunctions based on well-aligned n-type TiO_2 nanowell arrays and p-type NiO mesoporous nanosheets. The utilization of TiO_2 nanowells instead of conventional anodic nanotube (NT) geometry is to ensure a shorter diffusion path and a faster photoresponse as a self-powered device. The introduction of NiO mesoporous nanosheets in a flower-like morphology remarkably enhances light absorption to generate more electron–hole pairs, privileges the interfacial charge carrier transfer and largely decreases the charge carrier recombination. The TiO_2/NiO PD enables a highly efficient, stable and visible-blind UV detector with excellent wavelength selectivity in a self-powered mode. It is noteworthy that the scale of the PD device is easily adjusted by the size of starting Ti metals for anodization, which guarantees its feasibility for scale-up in a large area. The strategy of constructing a TiO_2-based p–n junction configuration with a large area into optoelectronic devices and the bottom-up low-cost device fabrication technique envisages a strong impact on many future applications, such as solar cells, image sensors, and photoelectronic switches.

Methodology

Preparation of anatase TiO_2 nanowells

The titanium foils (99.7% purity, 0.25 mm thick, Sigma Aldrich) were ultrasonically cleaned in acetone, ethanol and deionized water successively, and then dried in a nitrogen stream. The preparation of TiO_2 NTs was carried out in a two-electrode electrochemical cell with a Pt gauze as the counter electrode.[41] The Ti working anode was pressed together with an Al foil against an O-ring, defining a working area of $\sim$1.766 cm^2 (diameter of 1.5 cm). The anodization process was carried out at 45 V for 7–9 h in the electrolyte containing 0.35 wt% NH_4F (85% lactic acid), and 10 vol% DMSO (dimethyl sulphoxide, >99%) using a Keithley 2450 Sourcemeter. The as-anodized film was peeled off by ultrasonicaton, leaving an ordered concave pattern in the Ti substrate to generate TiO_2 nanowell layers. Then, the as-exposed nanowell substrate was thermally treated at 450 °C in air for 2 h.

Synthesis of TiO_2/NiO heterostructures

In a typical process (Scheme 1), nickel chloride ($NiCl_2{\cdot}6H_2O$, 0.24 mmol) and urea (CH_4N_2O, 4.8 mmol) were dissolved in 100 mL of distilled water and stirred for 30 min in a glass bottle with a blue lid. The anatase TiO_2 nanowells on Ti metal were used directly as the substrate and placed at the bottom of the bottle. Then the mixed solution was kept in an electric oven, heated at 90 °C for 24 h and then cooled to room temperature naturally. Finally, the substrate was washed with distilled water and ethanol, respectively, and dried at 80 °C for 6 h to produce TiO_2/Ni(OH)$_2$ hybrid structures. To obtain TiO_2/NiO heterostructures, the as-prepared sample was heated to 450 °C at a rate of 3 °C min^{-1} in air and kept at 450 °C for 2 h. Finally, two silver pastes with small area ($\approx$0.003 cm^2) were doctoral-bladed onto the sample as two electrodes to construct PD device. For comparison, anodic TiO_2 NTs on Ti foil were used as the substrates to produce TiO_2 NTs/NiO composites instead of TiO_2 nanowell substrates *via* a similar hydrothermal process, and the composites were annealed in air at 450 °C for 2 h.

Analysis instruments

Sample morphologies were characterized using a field-emission scanning electron microscope (FESEM, JSM-6701F) and a transmission electron microscope (TEM, TECNAI G^2 S-TWIN). X-ray diffraction (XRD) patterns were collected on a Bruker D8-A25 diffractometer using Cu K_α radiation (λ = 1.5405 Å). The X-ray photoelectron spectroscopy (XPS) spectra of the samples were recorded using a Perkin Elmer PHI 5000 C ESCA system equipped with a hemispherical electron energy analyzer, and the Mg-Kα (1253.6 eV) anode was operated at 14 kV and 20 mA. The optical properties were investigated by optical diffuse absorption spectra using a UV-vis spectrophotometer (Hitachi U-4100) with an integrating sphere attachment.

Photoelectric measurements

The photoelectric performance was analysed using a program-controlled semiconductor characterization system (Keithley 4200, USA). A 300 W xenon arc lamp and a monochromator with a series of band pass filters were used to produce the monochromatic light. The light intensity was measured using a NOVA II power meter (OPHIR photonics). The spectral photoresponse was measured from 280 to 600 nm. All the measurements were performed at room temperature under ambient conditions.

Results and discussion

The typical scanning electron microscopy (SEM) images of the different TiO_2-based nanostructures are presented in Fig. 1. The anodized TiO_2 NT arrays show a top-opened tubular morphology in a self-organization manner with an average outer tube diameter of approximately 205 nm (Fig. 1a). All the tubes are

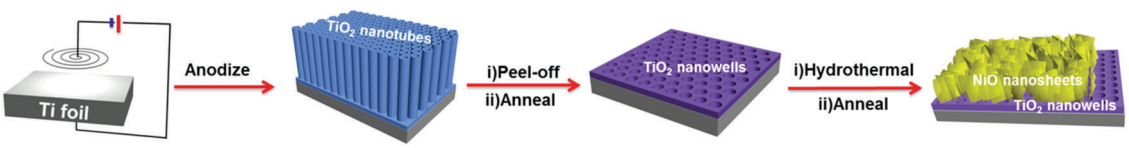

Scheme 1 Illustration of the preparation processes of TiO_2/NiO hybrids.

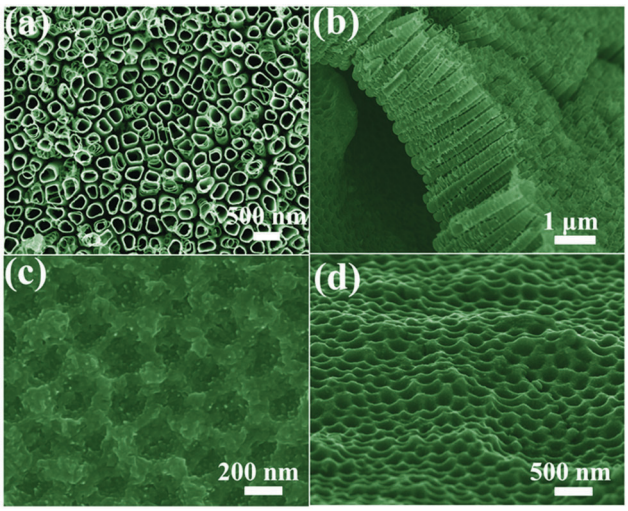

Fig. 1 (a and c) Plane-view and (b and d) side-view SEM images of TiO_2 nanotube arrays and TiO_2 nanowells, respectively.

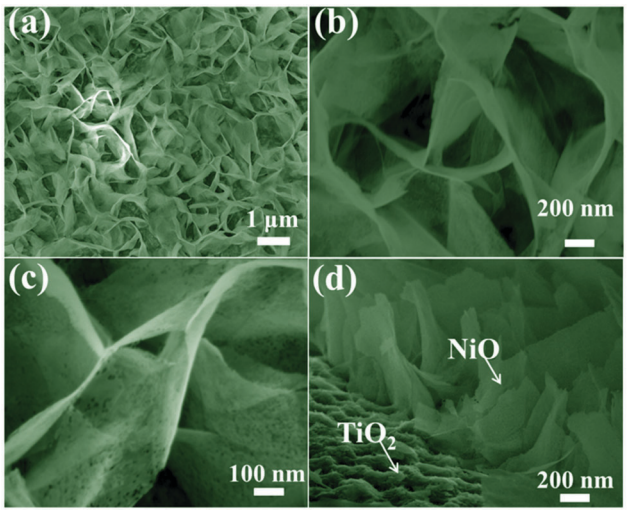

Fig. 2 (a–c) Plane-view and (d) side-view SEM images of TiO_2/NiO hybrids.

arranged perpendicular to the Ti substrate with a film thickness of ~2.53 μm (Fig. 1b). As the anodized nanotubes are amorphous,[42–44] they can be easily removed in an ultrasonication bath, leaving behind the highly ordered shallowed nanoconcave patterns on the Ti foil surface, *i.e.*, TiO_2 nanowells, as shown in Fig. 1c and d from both plane- and lateral-views. The TiO_2 nanowells demonstrate two-dimensional periodicity without cracking, with an average diameter of 200 nm. The thickness of the TiO_2 nanowell film is approximately 145 nm (Fig. S1, ESI†), which is promising for charge carrier transportation in the lateral direction owing to a shorter diffusion pathway compared to TiO_2 NT arrays and beneficial for faster photodetection.[19] In addition, as the nanoconcaved structural basis is easily formed by a facile electrochemical method, the scale of the PD devices can be readily adjusted by the size of Ti foils, which guarantees its feasibility for scale-up in an economic way.

The structural morphologies of TiO_2 nanowell/NiO nanosheet heterostructures (namely TiO_2/NiO hybrids below) are displayed in Fig. 2. The thin layers of NiO nanosheets are grown homogeneously on top of the TiO_2 nanowell surface assembled in the form of an interconnected network to form a flower-like morphology. This rationalized configuration is beneficial for the NiO/TiO_2 interfacial active reaction sites to be fully exposed to UV light, which helps harvest more light to enhance the generation of electron–hole pairs. Interestingly, it can be readily observed that numerous mesopores are created in the sheet-like NiO films through dehydration after sintering as indicated from the high-resolution SEM images in Fig. 2c, which is also favourable for more light intake by the underneath TiO_2. From the cross-sectional SEM images in Fig. 2d, each NiO nanosheet grows like a flower petal attached to the surface of TiO_2 nanowells with mean height approximately 700 nm. Transmission electron microscopy (TEM) images show more detailed information on the morphological and structural features of NiO as depicted in Fig. 3. The NiO nanosheets possess a large number of mesopores with diameters smaller than 10 nm, in good agreement with the SEM results in Fig. 2. The distinct lattice fringes correspond well to the (111) plane of cubic phase NiO with a spacing of 0.25 nm, supported by the high-resolution TEM image in Fig. 3a_2. Selected area electron diffraction (SAED) patterns (Fig. 3b_2) show a series of bright concentric rings, which represent the polycrystalline nature of NiO. With careful calculations, the first three diffraction rings

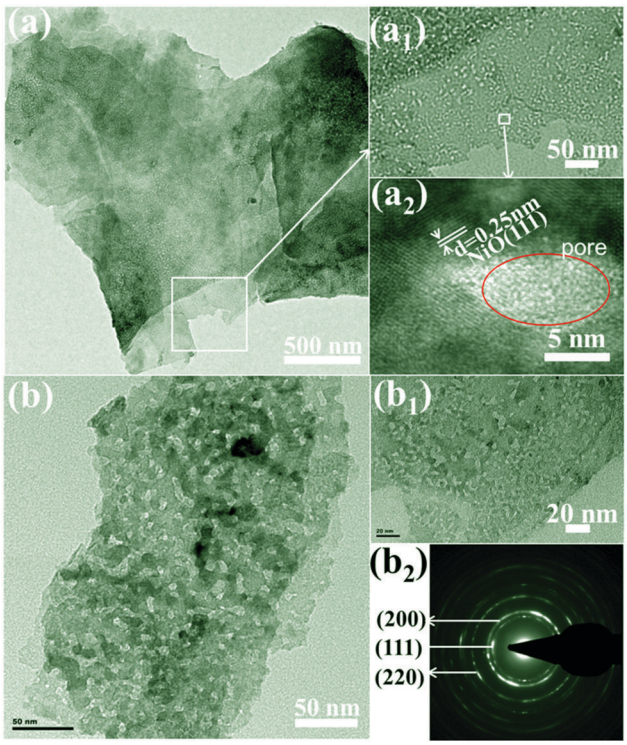

Fig. 3 (a and b) TEM images of mesoporous NiO nanosheets and (a_1 and b_1) their corresponding magnification images. (a_2) HRTEM images with lattice fringes designated by the white square in (a_1). (b_2) The selected area electron diffraction (SAED) patterns of NiO nanosheets.

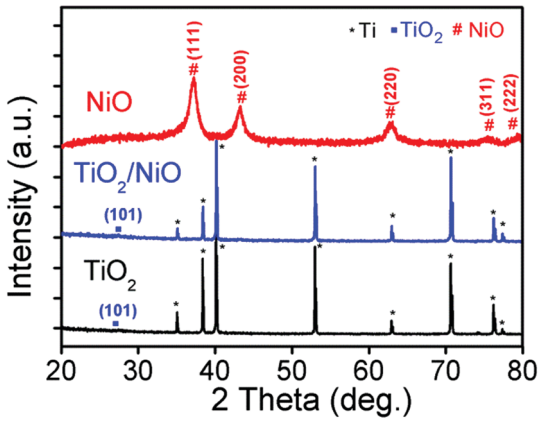

Fig. 4 XRD patterns of TiO_2 nanowells, NiO nanosheets and TiO_2/NiO hybrids.

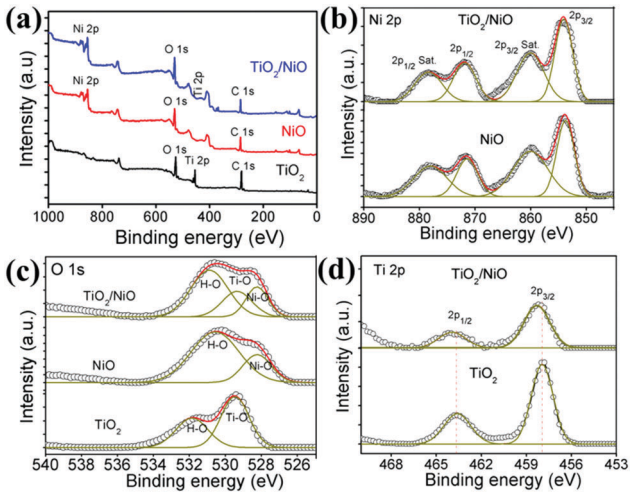

Fig. 5 XPS spectra of TiO_2 nanowells, NiO nanosheets and TiO_2/NiO hybrids: (a) survey scan, (b) Ni 2p, (c) O 1s, (d) Ti 2p XPS spectrum.

(from the inside to the outside) are interpreted as plane (111), (200) and (220) reflections of NiO, respectively.

X-ray diffraction (XRD) patterns of TiO_2 nanowells and TiO_2/NiO hybrids are displayed in Fig. 4. A major peak centred at 25.3°, assigned to the (101) facet of anatase TiO_2 (JCPDS card no. 21-1272), can be observed for both TiO_2 and TiO_2/NiO hybrids. Other peaks agreed well with Ti metal (JCPDS no. 1-1197) are so strong and sharp that the signals for NiO in the TiO_2/NiO hybrids are undetectable. As a result, we intentionally scratched off NiO from the Ti substrate and then performed XRD on the powdery sample. The results show that five broad diffraction peaks are indexed at 2θ = 37.2°, 43.2°, 62.8°, 75.5° and 79.4°, which correspond to the (110), (200), (220), (311), and (222) reflections of the NiO cubic phase (JCPDS no. 47-1049) with lower crystallinity,[39] which further confirmed the successful fabrication of NiO onto the TiO_2 surface on a Ti substrate.

X-ray photoelectron spectroscopy (XPS) analysis was performed to further study the chemical composition and the oxidation states of the as-prepared samples. Fig. 5a shows the survey XPS spectra of TiO_2/NiO hybrids, where the peaks of Ti are from TiO_2, and the Ni peak indicates the presence of NiO. The C element could be originated from the adventitious carbon-based contaminant, and the binding energy for the C 1s peak at 284.6 eV was used as the reference for calibration. The high resolution XPS spectra for the Ni 2p peak of the pure NiO sample and TiO_2/NiO hybrids are indicated in Fig. 5b. Both show two major peaks centred at ~853.9 and 871.6 eV with a spin-energy separation of 17.7 eV, corresponding to Ni $2p^{3/2}$ and Ni $2p^{1/2}$, respectively, accompanied by extra two sets of peaks located at higher binding-energy sides being correlated with their satellite peaks.[15] The typical characteristic of Ni in Ni–O bonds undoubtedly verifies the existence of NiO in TiO_2/NiO hybrids, consistent with the XRD results. Fig. 5c compares the high resolution O 1s XPS spectra of TiO_2 nanowells, NiO nanosheets and TiO_2/NiO hybrids. Characteristic peaks of both Ti–O–Ti[45,46] and Ni–O[47] groups can be detected in the TiO_2/NiO hybrids, also confirming the successful NiO loading onto TiO_2 nanowells. The dominant OH groups for TiO_2/NiO hybrids are found at 530.9 eV with high intensity mainly arising from the incomplete dehydration of $Ni(OH)_2$ at 450 °C.[48] The spin-energy separation of ~5.8 eV between Ti $2p^{1/2}$ (463.6 eV) and Ti $2p^{3/2}$ (457.9 eV) peaks indicates a normal chemical state of Ti^{4+} from anatase TiO_2 species in the TiO_2 nanowell sample (Fig. 5d).[46] While TiO_2/NiO hybrids exhibit a binding energy shift towards higher energy by 0.4 eV for Ti 2p, which is possibly caused by the introduction of NiO into the hybrid system through the formation of p–n junctions between NiO and TiO_2.[37,38] A decrease of the electron density of Ti^{4+} in the TiO_2/NiO hybrids is possibly due to the electron transfer from TiO_2 to the more electronegative NiO.[49,50]

The optical properties of TiO_2 nanowells and TiO_2/NiO hybrids are determined by UV-vis diffuse absorption spectra as shown in Fig. 6. Interestingly, both samples exhibit strong light absorption in the visible range (400–700) due to their selective light absorption of the photonic bandgaps (periodicity of nanoconcaved patterns in the Ti surface), leading to colorful sample appearances, and could be possibly useful in preparing photonic crystal materials.[42] The color of TiO_2 nanowells changes from purple to blue after hybridizing with NiO nanosheets (insets in Fig. 6a). The broad absorption peak centered at 495 nm for TiO_2 nanowells correspondingly shifts to 650 nm for TiO_2/NiO hybrids.

While in the UV-range (220–400 nm), the TiO_2/NiO hybrids exhibit a higher absorption in contrast to pristine TiO_2 nanowells, suggesting excellent UV light absorption of the composite. The energy band gap (E_g) can be estimated by the conventional Tauc equation:[51–53]

$$\alpha h\nu = A(h\nu - E_g)^{n/2} \quad (1)$$

where α is the absorption coefficient; $h\nu$ is the photon energy; A is the constant; n = 1 for a directly allowed transition and n = 4 for an indirectly allowed transition. The corresponding Kubelka–Munk transformed spectra are shown in Fig. 6b, where the slopes of the tangents on the horizontal axis are bandgap energies.

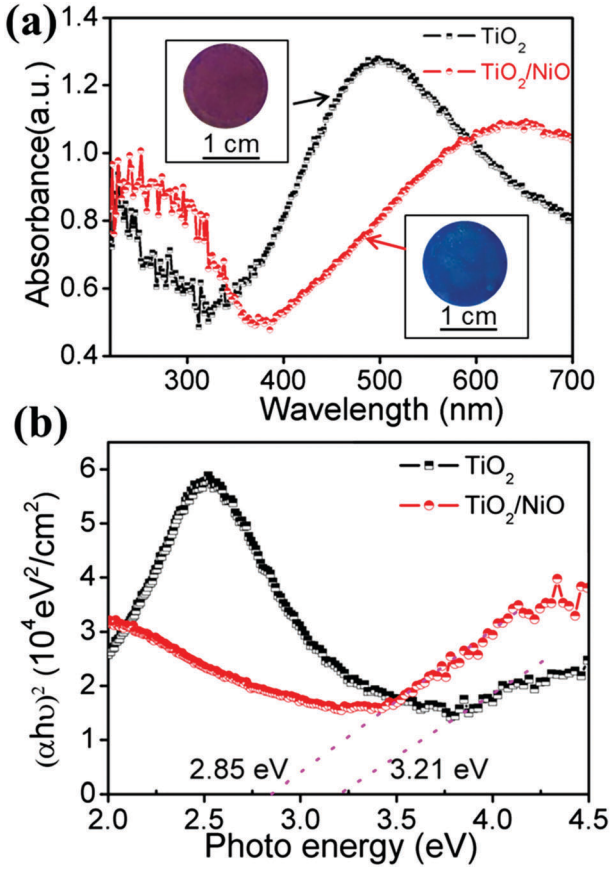

Fig. 6 (a) UV-vis diffuse absorption spectra and (b) the corresponding plot analysis of the optical band gap of TiO_2 nanowells and TiO_2/NiO hybrids. Insets in (a) show the optical graphs.

The calculated E_g is estimated to be about 3.21 eV for TiO_2 nanowells (corresponding to the absorption edge of ~386 nm) and ~2.85 eV for TiO_2/NiO hybrids (corresponding to the absorption edge of ~435 nm). The decreased bandgap of composites results in enhancement of light absorption, suggesting a positive effect by the introduction of NiO species.

The electrical and UV detection properties of PDs were carefully examined using a two-probe method under ambient conditions and monochromatic illumination based on TiO_2 nanowells, pure NiO nanosheets on glass substrates and TiO_2/NiO hybrids, and the results are shown in Fig. S2 (ESI†) and Fig. 7. The symmetric current–voltage (*I–V*) characteristics under dark reveal the existence of a Schottky junction owing to the Ag/TiO_2 contacts for the TiO_2 nanowell detector (Fig. S2a, ESI†). It is noteworthy that the *M–S* type configuration herein has no self-powered features. For a pure NiO PD, the linear *I–V* curve under dark indicates good ohmic contacts between Ag electrodes and the NiO sample (Fig. S2b, ESI†). No photoresponse can be detected upon 350 nm light illumination. Interestingly, the *I–V* curves of the TiO_2/NiO hybrids PD feature an excellent photovoltaic property with a short-circuit current of 0.65 nA and an open circuit voltage V_{oc} = 0.47 V (Fig. 7a). The high V_{oc} of the hybrid PD is the main result of p–n junctions at the NiO and TiO_2 interface, acting as a driving force to separate

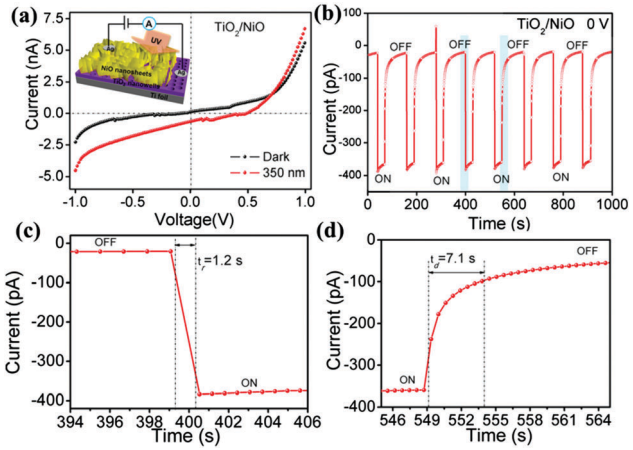

Fig. 7 (a) Typical *I–V* curves for TiO_2/NiO hybrids PD. (b) *I–t* curves during light on–off switching tests at 0 V bias with 350 nm illumination. (c and d) Enlarged portions of a 395–405 s range and a 545–565 s range corresponding to light-off to light-on and light-on to light-off transitions, respectively. Inset in (a) shows the device structure.

the photogenerated electron–hole pairs and produces photocurrent. Therefore, the device can work in a self-powered mode without any external power supply.

Repeatability and response speed are the key parameters to examine the capability of a PD. Fig. 7b shows the time-dependent photocurrent responses illuminated by 350 nm UV light at 0 V bias for TiO_2/NiO hybrids PD, which represents good stability and reproducibility without notable photocurrent-decay. Two distinct states can be readily observed to reveal the response and recovery speed of the hybrid PD, *i.e.*, the on-state under light illumination and the off-state in the dark, respectively. The detected photocurrent at the on-state is ~375 pA and the dark current at the off-state is ~25 pA (Fig. 7b). The photo-to-current ratio $((I_{light} - I_{dark})/I_{dark})$ is estimated to be ~14, suggesting a good photosensitivity as a self-powered device. A cliffy rise and decay can be clearly seen in the enlarged portions of a 395–405 s range and a 545–565 s range corresponding to the on-state and off-state, respectively, as displayed in Fig. 7c and d. The rise time τ_r (from 10 to 90% of the maximum photocurrent) and decay time τ_d (from 90 to 10% of the maximum photocurrent) are estimated to be 1.2 s and 7.1 s, respectively, for the TiO_2/NiO hybrids PD at zero bias (Table 1), which are comparable to those of other self-powered PDs.

The spectral responsivity (R_λ) is a critical parameter to determine the sensitivity of optoelectronic devices.[23,54] A larger R_λ represents a higher sensitivity and is expressed as the following equation:

$$R_\lambda = \Delta I/(PS) \quad (2)$$

where ΔI is the difference between the photocurrent and the dark current, P is the light power, S is the irradiated area on the sample, λ is the exciting wavelength. The calculated R_λ is as high as 42 μA W^{-1} under light illumination of 350 nm (a light intensity of 1.2 mW cm^{-2}) at 0 V bias as shown in Fig. 8a. The self-powered TiO_2/NiO hybrids PD is intrinsically "visible-light-blind" with a

Table 1 Comparison of the characteristic parameters of different photodetectors

Photodetector	Wavelength (nm)	Power density	Bias (V)	Photocurrent	Rise time	Decay time	Ref.
TiO_2 nanotubes	320	—	3	53 μA	min	min	19
Ni/TiO_2/Ni	250	15 μW m^{-2}	5	52.91 μA	13.34 ms	11.43 s	55
SnO_2/NiO	254	8 W	5	—	17 s	9 s	13
ZnO/NiO	365	—	−3	450 μA	12.7 s	6.4 s	15
ZnO/SnO_2	300	0.45 mW cm^{-2}	10	7.9 nA	32.2 s	7.8 s	56
Carbon/ZnO	355	0.58 mW cm^{-2}	0	2 nA	~1 s	< 20 s	57
Graphene/ZnO	365	1.3 mW m^{-2}	0	6.7 nA	3 s	0.5 s	58
Polyaniline/MgZnO	250	130 μW m^{-2}	0	15 pA	< 0.3 s	< 0.3 s	59
Cu Nanowire/ZnO	360	0.8 mW m^{-2}	0	70 pA	< 0.5 s	> 30 s	60
TiO_2/Si	365	11.2 μW m^{-2}	0	~4 nA	—	> 10 s	61
TiO_2/NiO	350	1.2 mW m^{-2}	0	375 pA	1.2 s	7.1 s	This work

cut-off wavelength of about 400 nm. Note that the responsivity drops 16 times at the visible light range as compared with the highest value (≈65 μA W^{-1} at 290 nm with a light intensity of 0.54 mW cm^{-2}).

Moreover, the detectivity D^* reflects the ability to detect the weak signals from the noise environment. By assuming that the shot noise from the dark current is the major contributor, it can be calculated as:[62–64]

$$D^* = R_\lambda/(2qI_dS)^{1/2} \quad (3)$$

where I_d is the dark current, q is the unit charge. Owing to the suppressed dark current, D^* is as high as 1.1×10^9 Jones at a wavelength of 350 nm. It is noteworthy that the high D^* in this work is acquired at zero bias, comparable to the recent-reported

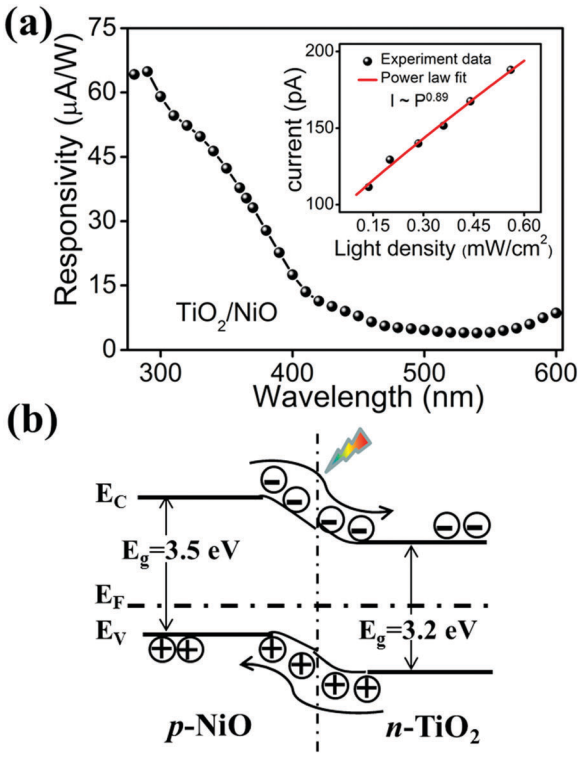

Fig. 8 (a) Spectral photoresponse for device TiO_2/NiO hybrids. (b) Diagram of the band alignment. Inset in (a) shows the light intensity dependence of photocurrent under 350 nm UV light illumination.

CuO/Si self-powered PD,[65] and also in contrast to high external bias reported previously.[2,66] The inset in Fig. 8a plots the variation of photocurrent generated by the self-powered TiO_2/NiO hybrids PD against light intensity upon 350 nm light illumination at 0 V bias. The photocurrent increases with light intensity, consistent with the fact that the charge carrier photogeneration efficiency is proportional to the absorbed photon flux. The nonlinear relationship between photocurrent and light intensity obeys the power law, $I \sim P^{0.89}$, suggesting a complex process of electron–hole generation, recombination, and trapping within the device.[19,23,67]

The self-powered behaviour of the hybrid PD in this study can be mainly ascribed to the following reasons. (1) The hybrid device configuration based on NiO mesoporous nanosheets stacking into a flower-like morphology on the TiO_2 surface (SEM images in Fig. 2) guarantees the interfacial active reaction sites between NiO and TiO_2 to be fully exposed to UV light, which takes most advantages of the junction area to enhance the generation of photoinduced electron–hole pairs. (2) The thin layer of TiO_2 nanowells (~145 nm-thick) enables faster charge carrier transportation in the lateral direction *via* a shorter diffusion pathway compared to TiO_2 NT arrays[19] and is beneficial for better photodetection. This is further verified by *I–V* measurements (Fig. S3, ESI†) performed on the p–n junction hybrid device based on conventional anodic TiO_2 NT arrays and NiO nanosheets (denoted TiO_2 NTs/NiO composites), which features rectifying characteristics due to the presence of p–n junctions. But it cannot function in self-powered mode at zero bias as the increased intercrystalline contacts as well as the extended electron transportation path in the vertical direction along the tubes result in faster electron–hole recombination when using vertically-oriented tubular geometry.[19,54,68,69]

Moreover, the photocurrent during UV light on–off switching tests measured at 1.0 V for the TiO_2 NTs/NiO composites PD is unstable with remarkable decay as well as slower response times (*i.e.*, τ_r = 3.5 s; τ_d = 12.2 s) (Fig. S4, ESI†), indicating that the device configuration plays a significant role in the photoelectric performance.

On the basis of the above experimental results and theoretical analysis, a proposed energy band structure diagram of the self-powered TiO_2/NiO hybrids PD is elucidated in Fig. 8b. When p-type NiO and n-type TiO_2 form a heterojunction, a depletion region is developed at the interface by carrier diffusion under

thermal equilibrium conditions, and it gives a built-in electric field which changes the band bending at the interface and provides a driving force for the separation of electrons and holes.[12,37,70] Upon above-bandgap light illumination, the photo-generated electron–hole pairs could be separated at a faster rate by the built-in electric field inside the depletion region. Forced by the electric field, the electrons are directed to the conduction band of the n-type TiO_2 while the holes are moved towards the valence band of the p-type NiO, leading to the generation of a photovoltaic current in the external circuit. In addition, the minority carriers generated within the diffusion length from the depletion region could also diffuse to the depletion region and be extracted by the built-in electric field. The photovoltage is a result of the energy difference between the Fermi levels of NiO and TiO_2 under illumination. This photovoltaic effect enables the current device to sense UV light without any external energy supply.

Conclusions

In summary, a novel type of self-powered UV PD is successfully achieved based on n-type TiO_2 nanowells and p-type NiO mesoporous nanosheets with a large area in a low-cost fabrication strategy. The TiO_2 nanowells are obtained *in situ* with periodically patterned nanoconcaves in the Ti substrate, which is beneficial for the separation of electron–hole pairs in the lateral direction, leading to better photoelectric performance compared to the conventional NT-based counterparts. The rationalized configuration of NiO flower-like stacking geometry makes the most use of the junction area for light absorption. The hybrid PD based on p–n junctions functions well in a self-powered mode with good responsivity, high stability and excellent wavelength selectivity. Note that the device scale can be easily adjusted by the size of the Ti starting material for anodization. This work presents us an effective and facile route for fabricating high performance self-powered PDs with a large area, suggesting potential applications in future optoelectronic devices without using external power supply.

Acknowledgements

The work was supported by the National Natural Science Foundation of China (Grant No. 51471051), Science and Technology Commission of Shanghai Municipality (15520720700), Shanghai Shu Guang Project (12SG01), the Programs for Professor of Special Appointment (Eastern Scholar) at Shanghai Institutions of Higher Learning. Part of the experimental work has been carried out in Fudan Nanofabrication Laboratory.

Notes and references

1 X. Liu, L. L. Gu, Q. P. Zhang, J. Y. Wu, Y. Z. Long and Z. Y. Fan, *Nat. Commun.*, 2014, **5**, 4007.
2 D. S. Tsai, K. K. Liu, D. H. Lien, M. L. Tsai, C. F. Kang, C. A. Lin, L. J. Li and J. H. He, *ACS Nano*, 2013, **7**, 3905–3911.
3 H. Lu, W. Tian, F. R. Cao, Y. L. Ma, B. K. Gu and L. Li, *Adv. Funct. Mater.*, 2016, **26**, 1296–1302.
4 S. M. Hatch, J. Briscoe and S. Dunn, *Adv. Mater.*, 2013, **25**, 867–871.
5 Z. Yang, M. Q. Wang, J. J. Ding, Z. W. Sun, L. Li, J. Huang, J. Liu and J. Y. Shao, *ACS Appl. Mater. Interfaces*, 2015, **7**, 21235–21244.
6 R. Kallol, P. Medini, G. Srijit, S. T Phanindra, R. Gopalakrishnan, R. Srinivasan and G. Arindam, *Nat. Nanotechnol.*, 2013, **8**, 826–830.
7 P. Irvin, Y. Ma, D. F. Bogorin, C. Cen, C. W. Bark, C. M. Folkman, C. B. Eom and J. Levy, *Nat. Photonics*, 2010, **4**, 849–852.
8 K. M. Kim, S. J. Song, G. H. Kim, J. Y. Seok, M. H. Lee, J. H. Yoon, J. Park and C. S. Hwang, *Adv. Funct. Mater.*, 2011, **21**, 1587–1592.
9 Y. Q. Bie, Z. M. Liao, H. Z. Zhang, G. R. Li, Y. Ye, Y. B. Zhou, J. Xu, Z. X. Qin, L. Dai and D. P. Yu, *Adv. Mater.*, 2011, **23**, 649–653.
10 H. Y. Chen, H. Liu, Z. M. Zhang, K. Hu and X. S. Fang, *Adv. Mater.*, 2016, **28**, 403–433.
11 H. Y. Chen, K. W. Liu, L. F. Hu, A. A. Al-Ghamdi and X. S. Fang, *Mater. Today*, 2015, **18**, 493–502.
12 L. Peng, L. F. Hu and X. S. Fang, *Adv. Funct. Mater.*, 2014, **24**, 2591–2610.
13 S. Huang, H. Wu, K. Matsubara, J. Cheng and W. Pan, *Chem. Commun.*, 2014, **50**, 2847–2850.
14 O. V. Bilousov, J. J. Carvajal, H. Geaney, V. Z. Zubialevich, P. J. Parbrook, O. Martinez, J. Jimenez, F. Diaz, M. Aguilo and C. O'Dwyer, *ACS Appl. Mater. Interfaces*, 2014, **6**, 17954–17964.
15 W. Dai, X. Pan, S. Chen, C. Chen, Z. Wen, H. Zhang and Z. Ye, *J. Mater. Chem. C*, 2014, **2**, 4606–4614.
16 M. S. Choi, D. Qu, D. Lee, X. Liu, K. Watanabe, T. Taniguchi and W. J. Yoo, *ACS Nano*, 2014, **8**, 9332–9340.
17 J. Briscoe, M. Stewart, M. Vopson, M. Cain, P. M. Weaver and S. Dunn, *Adv. Energy Mater.*, 2012, **2**, 1261–1268.
18 Y. Jin, J. Wang, B. Sun, J. C. Blakesley and N. C. Greenham, *Nano Lett.*, 2008, **8**, 1649–1653.
19 G. Liu, N. Hoivik, X. Wang, S. Lu, K. Wang and H. Jakobsen, *Electrochim. Acta*, 2013, **93**, 80–86.
20 X. S. Fang, J. Yan, L. Hu, H. Liu and P. S. Lee, *Adv. Funct. Mater.*, 2012, **22**, 1613–1622.
21 X. S. Fang, Y. Bando, M. Liao, U. K. Gautam, C. Zhi, B. Dierre, B. Liu, T. Zhai, T. Sekiguchi, Y. Koide and D. Golberg, *Adv. Mater.*, 2009, **21**, 2034–2039.
22 H. Liu, L. Hu, K. Watanabe, X. Hu, B. Dierre, B. Kim, T. Sekiguchi and X. S. Fang, *Adv. Funct. Mater.*, 2013, **23**, 3701–3709.
23 H. Liu, N. Gao, M. Liao and X. S. Fang, *Sci. Rep.*, 2015, **5**, 7716.
24 H. Li, Z. Chen, C. K. Tsang, Z. Li, X. Ran, C. Lee, B. Nie, L. Zheng, T. Hung, J. Lu, B. Pan and Y. Y. Li, *J. Mater. Chem. A*, 2014, **2**, 229–236.
25 L. X. Zheng, H. Cheng, F. Liang, S. Shu, C. K. Tsang, H. Li, S.-T. Lee and Y. Y. Li, *J. Phys. Chem. C*, 2012, **116**, 5509–5515.
26 P. Roy, S. Berger and P. Schmuki, *Angew. Chem., Int. Ed.*, 2011, **50**, 2904–2939.

27 Q. Z. J. Zou, K. Huang and N. Marzari, *J. Phys. Chem. C*, 2010, **114**, 10725–10729.
28 T. Y. Tsai, S. J. Chang, W. Y. Weng, C. L. Hsu, S. H. Wang, C. J. Chiu, T. J. Hsueh and S. P. Chang, *J. Electrochem. Soc.*, 2012, **159**, J132–J135.
29 Q. Zhu, C. Xie, H. Li, C. Yang and D. Zeng, *Nano Energy*, 2014, **9**, 252–263.
30 J. Zhou, L. Chen, Y. Wang, Y. He, X. Pan and E. Xie, *Nanoscale*, 2015, **8**, 50–73.
31 L. Han, L. Bai and S. Dong, *Chem. Commun.*, 2014, **50**, 802–804.
32 H. Wang, G. Yi, X. Zu, X. Jiang, Z. Zhang and H. Luo, *Mater. Lett.*, 2015, **138**, 204–207.
33 Y. H. Ko, G. Nagaraju and J. S. Yu, *Nanoscale*, 2015, **7**, 2735–2742.
34 P. N. Ni, C. X. Shan, S. P. Wang, X. Y. Liu and D. Z. Shen, *J. Mater.Chem. C*, 2013, **1**, 4445–4449.
35 Y. Kim do, J. Ryu, J. Manders, J. Lee and F. So, *ACS Appl. Mater. Interfaces*, 2014, **6**, 1370–1374.
36 X. Yu, J. Zhang, Z. Zhao, W. Guo, J. Qiu, X. Mou, A. Li, J. P. Claverie and H. Liu, *Nano Energy*, 2015, **16**, 207–217.
37 M. Wang, Y. Hu, J. Han, R. Guo, H. Xiong and Y. Yin, *J. Mater. Chem. A*, 2015, **3**, 20727–20735.
38 R. Liu, H. Yoshida, S.-i. Fujita and M. Arai, *Appl. Catal., B*, 2014, **144**, 41–45.
39 G. Li, H. Hu, Q. Zhu and Y. Yu, *RSC Adv.*, 2015, **5**, 101247–101256.
40 J.-H. Kim, K. Zhu, Y. Yan, C. L. Perkins and A. J. Frank, *Nano Lett.*, 2010, **10**, 4099–4104.
41 H. E. Prakasam, K. Shankar, M. Paulose, O. K. Varghese and C. A. Grimes, *J. Phys. Chem. C*, 2007, **111**, 7235–7241.
42 Z. Li, Y. Xin and Z. Zhang, *Nanoscale*, 2015, **7**, 19894–19898.
43 L. X. Zheng, S. C. Han, H. Liu, P. P. Yu and X. S. Fang, *Small*, 2016, **12**, 1527–1536.
44 D. Wang, Y. Liu, C. Wang, F. Zhou and W. Liu, *ACS Nano*, 2009, **3**, 1249–1257.
45 X. Lu, G. Wang, T. Zhai, M. Yu, J. Gan, Y. Tong and Y. Li, *Nano Lett.*, 2012, **12**, 1690–1696.
46 L. Zheng, C. Wang, Y. Dong, H. Bian, T. F. Hung, J. Lu and Y. Y. Li, *Appl. Surf. Sci.*, 2015, **362**, 399–405.
47 C. Hu, K. Chu, Y. Zhao and W. Y. Teoh, *ACS Appl. Mater. Interfaces*, 2014, **6**, 18558–18568.
48 S. I. Kim, J. S. Lee, H. J. Ahn, H. K. Song and J. H. Jang, *ACS Appl. Mater. Interfaces*, 2013, **5**, 1596–1603.
49 J. Liu, L. Zhang, N. Li, Q. Tian, J. Zhou and Y. Sun, *J. Mater. Chem. A*, 2015, **3**, 706–712.
50 L. Wei, Y. Chen, Y. Lin, H. Wu, R. Yuan and Z. Li, *Appl. Catal., B*, 2014, **144**, 521–527.
51 Y. Wang, Y. N. Zhang, G. Zhao, H. Tian, H. Shi and T. Zhou, *ACS Appl. Mater. Interfaces*, 2012, **4**, 3965–3972.
52 Z. Jiang, C. Zhu, W. Wan, K. Qian and J. Xie, *J. Mater. Chem. A*, 2016, **4**, 1806–1818.
53 J. Ma, C. Wang and H. He, *Appl. Catal., B*, 2016, **184**, 28–34.
54 L. Li, X. S. Fang, T. Zhai, M. Liao, U. K. Gautam, X. Wu, Y. Koide, Y. Bando and D. Golberg, *Adv. Mater.*, 2010, **22**, 4151–4156.
55 X. Kong, C. Liu, W. Dong, X. Zhang, C. Tao, L. Shen, J. Zhou, Y. Fei and S. Ruan, *Appl. Phys. Lett.*, 2009, **94**, 123502.
56 W. Tian, T. Zhai, C. Zhang, S. L. Li, X. Wang, F. Liu, D. Liu, X. Cai, K. Tsukagoshi, D. Golberg and Y. Bando, *Adv. Mater.*, 2013, **25**, 4625–4630.
57 Z. Zhan, L. Zheng, Y. Pan, G. Sun and L. Li, *J. Mater. Chem.*, 2012, **22**, 2589–2595.
58 B. D. Boruah, A. Mukherjee and A. Misra, *Nanotechnology*, 2016, **27**, 095205.
59 H. Y. Chen, P. P. Yu, Z. M. Zhang, F. Teng, L. X. Zheng, K. Hu and X. S. Fang, *Small*, 2016, DOI: 10.1002/smll.201601913.
60 F. Teng, L. X. Zheng, K. Hu, H. Y. Chen, Y. M. Li, Z. M. Zhang and X. S. Fang, *J. Mater. Chem. C*, 2016, **4**, 8416–8421.
61 Z. Song, H. Zhou, P. Tao, B. Wang, J. Mei, H. Wang, S. Wen, Z. Song and G. Fang, *Mater. Lett.*, 2016, **180**, 179–183.
62 B. Zhao, F. Wang, H. Chen, Y. Wang, M. Jiang, X. S. Fang and D. Zhao, *Nano Lett.*, 2015, **15**, 3988–3993.
63 L. Shen, Y. Fang, H. Wei, Y. Yuan and J. Huang, *Adv. Mater.*, 2016, **28**, 2043–2048.
64 C. Ma, Y. Shi, W. Hu, M.-H. Chiu, Z. Liu, A. Bera, F. Li, H. Wang, L.-J. Li and T. Wu, *Adv. Mater.*, 2016, **28**, 3683–3689.
65 Q. Hong, Y. Cao, J. Xu, H. Lu, J. He and J. L. Sun, *ACS Appl. Mater. Interfaces*, 2014, **6**, 20887–20894.
66 G. Su, V. G. Hadjiev, P. E. Loya, J. Zhang, S. Lei, S. Maharjan, P. Dong, P. M. Ajayan, J. Lou and H. Peng, *Nano lett.*, 2014, **15**, 506–513.
67 H. Liu, Z. Zhang, L. Hu, N. Gao, L. Sang, M. Liao, R. Ma, F. Xu and X. S. Fang, *Adv. Opt. Mater.*, 2014, **2**, 771–778.
68 F. Xia, T. Mueller, Y.-M. Lin, A. Valdes Garcia and P. Avouris, *Nat. Nanotechnol.*, 2010, **4**, 839–843.
69 L. Wang, W. Yang, H. Chong, L. Wang, F. Gao, L. Tian and Z. Yang, *RSC Adv.*, 2015, **5**, 52388–52394.
70 K. Khun, Z. H. Ibupoto and M. Willander, *Phys. Status Solidi A*, 2013, **210**, 2720–2724.